The CARMENES search for exoplanets around M dwarfs

Radial-velocity variations of active stars in visual-channel spectra[⋆]

L. Tal-Or[1], M. Zechmeister[1], A. Reiners[1], S. V. Jeffers[1], P. Schöfer[1], A. Quirrenbach[2], P. J. Amado[3], I. Ribas[4,5],
J. A. Caballero[6], J. Aceituno[3,7], F. F. Bauer[1], V. J. S. Béjar[8,9], S. Czesla[10], S. Dreizler[1], B. Fuhrmeister[10],
A. P. Hatzes[11], E. N. Johnson[1], M. Kürster[12], M. Lafarga[4,5], D. Montes[13], J. C. Morales[4,5], S. Reffert[2], S. Sadegi[2],
W. Seifert[2], and D. Shulyak[1]

[1] Institut für Astrophysik, Georg-August-Universität, Friedrich-Hund-Platz 1, 37077 Göttingen, Germany
  e-mail: levtalor@astro.physik.uni-goettingen.de
[2] Landessternwarte, Zentrum für Astronomie der Universität Heidelberg, Königstuhl 12, 69117 Heidelberg, Germany
[3] Instituto de Astrofísica de Andalucía (IAA-CSIC), Glorieta de la Astronomía s/n, 18008 Granada, Spain
[4] Institut de Ciències de l'Espai (ICE, CSIC), Campus UAB, c/ de Can Magrans s/n, 08193 Bellaterra, Barcelona, Spain
[5] Institut d'Estudis Espacials de Catalunya (IEEC), 08034 Barcelona, Spain
[6] Centro de Astrobiología (CSIC-INTA), ESAC Campus, Camino Bajo del Castillo s/n, 28692 Villanueva de la Cañada, Madrid,
  Spain
[7] Centro Astronómico Hispano-Alemán (CSIC-MPG), Observatorio Astronómico de Calar Alto, Sierra de los Filabres-04550 Gérgal,
  Almería, Spain
[8] Instituto de Astrofísica de Canarias, Vía Láctea s/n, 38205 La Laguna, Tenerife, Spain
[9] Departamento de Astrofísica, Universidad de La Laguna, 38206 La Laguna, Tenerife, Spain
[10] Hamburger Sternwarte, Gojenbergsweg 112, 21029 Hamburg, Germany
[11] Thüringer Landessternwarte Tautenburg, Sternwarte 5, 07778 Tautenburg, Germany
[12] Max-Planck-Institut für Astronomie, Königstuhl 17, 69117 Heidelberg, Germany
[13] Departamento de Física de la Tierra y Astrofísica & UPARCOS-UCM (Unidad de Física de Partículas y del Cosmos de la UCM),
  Facultad de Ciencias Físicas, Universidad Complutense de Madrid, 28040 Madrid, Spain

ABSTRACT

Context. Previous simulations predicted the activity-induced radial-velocity (RV) variations of M dwarfs to range from ∼1 cm s^{-1} to ∼1 km s^{-1}, depending on various stellar and activity parameters.
Aims. We investigate the observed relations between RVs, stellar activity, and stellar parameters of M dwarfs by analyzing CARMENES high-resolution visual-channel spectra (0.5–1 μm), which were taken within the CARMENES RV planet survey during its first 20 months of operation.
Methods. During this time, 287 of the CARMENES-sample stars were observed at least five times. From each spectrum we derived a relative RV and a measure of chromospheric Hα emission. In addition, we estimated the chromatic index (CRX) of each spectrum, which is a measure of the RV wavelength dependence.
Results. Despite having a median number of only 11 measurements per star, we show that the RV variations of the stars with RV scatter of >10 m s^{-1} and a projected rotation velocity $v \sin i$ > 2 km s^{-1} are caused mainly by activity. We name these stars "active RV-loud stars" and find their occurrence to increase with spectral type: from ∼3% for early-type M dwarfs (M0.0–2.5 V) through ∼30% for mid-type M dwarfs (M3.0–5.5 V) to >50% for late-type M dwarfs (M6.0–9.0 V). Their RV-scatter amplitude is found to be correlated mainly with $v \sin i$. For about half of the stars, we also find a linear RV–CRX anticorrelation, which indicates that their activity-induced RV scatter is lower at longer wavelengths. For most of them we can exclude a linear correlation between RV and Hα emission.
Conclusions. Our results are in agreement with simulated activity-induced RV variations in M dwarfs. The RV variations of most active RV-loud M dwarfs are likely to be caused by dark spots on their surfaces, which move in and out of view as the stars rotate.

Key words. stars: late-type – stars: activity – stars: rotation – techniques: radial velocities

1. Introduction

Precise radial-velocity (PRV) surveys of well-defined stellar samples constitute an important pathway to characterize their inner planetary systems (e.g., Winn & Fabrycky 2015). The first

---

[⋆] The data presented in Figs. 5 and A.1 are only available in electronic form at the CDS via anonymous ftp to cdsarc.u-strasbg.fr (130.79.128.5) or via http://cdsarc.u-strasbg.fr/viz- bin/qcat?J/A+A/614/A122

PRV surveys focused mainly on solar-type stars (e.g., Campbell et al. 1988), and largely overlooked M dwarfs, the most abundant type of stars in our Galaxy. There were two main reasons for doing so. First, M dwarfs are intrinsically fainter than solar-type stars, particularly in visible light, where most PRV instruments were operating. Second, a large fraction of M dwarfs are fast rotating and magnetically active, two phenomena that are linked to each other (e.g., Reiners et al. 2012; Newton et al. 2017; Jeffers et al. 2018). Fast rotation and activity complicate the detection

of planetary-induced radio-velocity (RV) signals (e.g., Saar & Donahue 1997; Hatzes 2002; Reiners et al. 2010; Barnes et al. 2011).

Recently the focus of PRV surveys has shifted slightly towards M dwarfs. The shift is driven by the desire to complement our picture of planetary occurrence rates around different type stars (e.g., Howard et al. 2012; Dressing & Charbonneau 2013), and by the ability of detecting low-mass habitable-zone planets around nearby stars with RV instruments of $\sim 1\,\mathrm{m\,s^{-1}}$ accuracy (e.g., Anglada-Escudé et al. 2016; Ribas et al. 2016). In the previous decade (Zechmeister et al. 2009) monitored the RVs of 40 M dwarfs with UVES at the VLT (Dekker et al. 2000). The largest PRV survey of M dwarfs to date was carried out by Bonfils et al. (2013), who monitored 102 southern hemisphere stars with HARPS (Mayor et al. 2003). A few additional surveys are either being planned or executed (Fischer et al. 2016). However, to use M-dwarf PRV surveys to their full extent, there is a need for efficient tools to distinguish between orbital- and activity-induced RV signals. Understanding the ways in which rotation and activity alter the measured RVs of M dwarfs is essential in developing such tools.

Stellar RVs are measured mainly from photospheric absorption lines. There are several activity-related phenomena that can cause variations in M-dwarf spectra. Inhomogeneities of the stellar photosphere, such as spots and faculae that corotate with the star, alter the shapes of absorption lines by changing the brightness and spectral appearance of parts of the stellar disk (e.g. Saar & Donahue 1997). Since these features are often accompanied by strong magnetic fields, they also cause Zeeman splitting of spectral lines (e.g., Semel 1989; Donati et al. 2006; Reiners & Basri 2007). Moreover, magnetically active regions suppress the convective blueshift of cool stars, leading to a net redshift of their spectra (e.g., Gray 2009). In addition, photospheric magnetic activity can induce chromospheric features such as filaments and plages, the latter being associated with line emission. The extreme cases of magnetically induced chromospheric activity are strong flares that could alter the entire spectral appearance of a star (e.g., Fuhrmeister et al. 2008).

To understand the impact of these phenomena on measured M-dwarf RVs, two complementary efforts are being made. The first is simulating the effects via forward modeling the spectra and RVs of active rotating stars. The second is measuring the RVs of active stars and trying to correlate the observed variations with various activity indicators, which could be derived either from the spectra themselves or from auxiliary simultaneous measurements.

Regarding forward modeling, Reiners et al. (2010) and Barnes et al. (2011) simulated the impact of active regions, such as cool spots, on RV measurements of M dwarfs over the wavelength range of 0.5–$2.2\,\mu\mathrm{m}$ for a wide variety of possible combinations of star and spot parameters. Both teams concluded that the flux contrast between the active regions and the unperturbed photosphere will induce RV-variation amplitudes that can range from $\sim 1\,\mathrm{cm\,s^{-1}}$ to $\sim 1\,\mathrm{km\,s^{-1}}$. These amplitudes depend on the specific parameters of the star and its spots, such as the spot-coverage fraction, the projected rotation velocity ($v \sin i$) of the star, its spectral type (SpT), and the spot-to-photosphere temperature contrast. For instance, they predicted higher RV amplitudes for higher spot-to-photosphere temperature contrasts ($\sim 1000\,\mathrm{K}$), while for low contrasts ($\sim 200\,\mathrm{K}$), they predicted a stronger decrease of RV

amplitudes when going from observations at $\sim 0.5\,\mu\mathrm{m}$ to observations at $\sim 1.0\,\mu\mathrm{m}$.

Reiners et al. (2013) estimated the additional impact that the Zeeman effect would have on active-star RVs. They concluded that in the wavelength range of 0.5–$2.3\,\mu\mathrm{m}$ it could be as large as the flux-contrast effect, depending on the strength of the magnetic fields that accompany the active regions. In contrast to RV variations caused by the flux-contrast effect of low temperature-contrast spots, the amplitude of RV variations caused by the Zeeman effect grows with wavelength. However, the actual impact of the effect on M-dwarf spectra is highly uncertain, mainly due to our limited knowledge of Landé g factors of molecular levels.

Convective-blueshift suppression by active regions would also impact RVs (e.g., Meunier et al. 2010). The impact of such convection suppression on solar-type RVs was studied in detail (e.g., Jeffers et al. 2014; Dumusque et al. 2014; Reiners et al. 2016; Meunier et al. 2017), and it was shown that it could reach a few times $10\,\mathrm{m\,s^{-1}}$. Assuming simple scaling relations, Kürster et al. (2003) estimated the impact of the suppression on M-dwarf RVs to be smaller by an order of magnitude.

In contrast to photospheric surface inhomogeneities, the direct effect of chromospheric emission variations on RVs has not yet been numerically addressed. This is most likely due to the relative difficulty of simulating chromospheric processes (Reiners 2009).

With regard to observations, several investigations have been published on activity-induced RV variations of M dwarfs, and on using different indicators to associate the variations with activity. The most widely used activity indicators in these works were variations in the average absorption-line shape, measured via the different moments of the cross-correlation function (CCF; e.g., Queloz et al. 2001), and variations of chromospheric emission lines, such as Ca II H&K and Hα. In addition, simultaneous (or contemporaneous) photometric time series were used to determine rotational periods (P_{rot}), and to trace activity-related phenomena (e.g., Bonfils et al. 2007; Anglada-Escudé et al. 2016).

Kürster et al. (2003) reported a correlation between Barnard's star RVs and variations in the Hα line. Bonfils et al. (2007) used photometric time series, as well as the chromospheric Ca II H&K and Hα emission lines, to attribute the 35-day RV signal of GJ 674 to stellar activity. Bonfils et al. (2013) also reported detecting a few periodic RV signals that correlated with at least one of their activity indicators: Ca II H&K, Hα, and the different moments of the CCF. Unfortunately, Bonfils et al. (2013) specifically excluded from their sample rapid rotators ($v \sin i > 6.5\,\mathrm{km\,s^{-1}}$), which would naturally be the most active stars in their volume-limited sample. Barnes et al. (2014) reported RV measurements of 15 M5–9 V stars, with many of them presenting activity-induced signals of up to $\sim 100\,\mathrm{m\,s^{-1}}$. Despite their low number and short time-span of observations (3–5 RVs per star, gathered in one week), they found significant correlations between RV-scatter amplitude, $v \sin i$, and chromospheric Hα activity. Finally, Suárez Mascareño et al. (2017b) reported detecting periodic activity-induced RV signals with amplitudes of 1–$10\,\mathrm{m\,s^{-1}}$ in 18 M0–5 V stars. Their results relied on several years of monitoring and some tens to hundreds RVs per star. They found a significant correlation of RV scatter with the chromospheric activity indicators Ca II H&K and Hα. However, only slowly rotating stars, with $20\,\mathrm{d} < P_{\mathrm{rot}} < 100\,\mathrm{d}$, were observed for this work.

The direct effect of strong chromospheric emission on RVs was reported only for a few M dwarfs. Reiners (2009) described a strong flare event in the M6 V star CN Leo, which was detected via a 0.9 dex enhancement of Hα emission. The flare was accompanied by an RV deviation of a few hundred m s^{-1}. However, flares with <0.4 dex changes in Hα emission did not result in RV deviations at the 10 m s^{-1} level. Barnes et al. (2014) reported tentative evidence for ~20 m s^{-1} RV excursions that might have been caused by flares on the M5.5 V star Proxima Centauri, but with a weak correlation with changes in Hα emission.

Out of the few dedicated PRV instruments that specifically aim at surveying nearby M dwarfs to detect their planets, CARMENES was the first to be on sky (Quirrenbach et al. 2016; Fischer et al. 2016, and references therein). Its sample is composed of >300 nearby northern hemisphere M-dwarfs, and covers the full range of M-dwarf SpT (M0–9 V). Fast-rotating and active stars were not explicitly excluded from the survey (Reiners et al. 2018b). Taking advantage of this large and highly diverse sample, we use the CARMENES visual-channel spectra to empirically investigate the relation between M-dwarf RVs, their rotation, and their activity. In particular, we focus on stars with $v \sin i > 2$ km s^{-1} and activity-induced RV variations of >10 m s^{-1}, which we call "active RV-loud stars".

The CARMENES survey is briefly presented in Sect. 2. Section 3 explains our data reduction, and RV and activity measurements. In Sect. 4 we present our sample of active RV-loud stars. Using this sample, we investigate the observed connection between RVs, stellar rotation, and stellar activity in Sect. 5, and we summarize our findings in Sect. 6.

2. CARMENES survey

The contents of the CARMENES-survey input catalog (Carmencita, Caballero et al. 2016a), are described by Alonso-Floriano et al. (2015), Cortés-Contreras et al. (2017), and Jeffers et al. (2018). Carmencita contains detailed information on about 2200 M dwarfs brighter than $J = 11.5$ mag that can be observed from Calar Alto (i.e., $\delta \gtrsim -23$ deg). Using the compiled information, the stars were prioritized, and 324 stars were selected for the CARMENES-survey sample.

The selected stars for the CARMENES sample were presented by Reiners et al. (2018b), who listed several stellar parameters for each survey star, including information on their $P_{\rm rot}$, $v \sin i$, and Hα emission. Stars with known stellar companions at less than 5 arcsec separation were excluded from the survey (Cortés-Contreras et al. 2017), but stars with known planetary systems were not (e.g., Trifonov et al. 2018). Although rapid rotation and strong magnetic activity degrade RV precision, stars with high $v \sin i$ values or strong Hα emission were not excluded from the survey.

Following a successful commissioning of the CARMENES instrument in October–December 2015, the CARMENES survey started in January 2016 (Quirrenbach et al. 2016). More than 7000 M-dwarf spectra were recorded during the first 20 months of operation. The median number of measurements per star was 11 166 stars were observed more than 10 times, and 60 stars were observed more than 30 times.

Despite providing high-quality spectra (e.g., Reiners et al. 2018b), during its first months of operations, the near-infrared channel (NIR) suffered from several systematic issues that prevented us from reaching an RV accuracy comparable to the visual channel (VIS). Some of these systematic issues are still under investigation. For this reason, only VIS spectra are used for this paper.
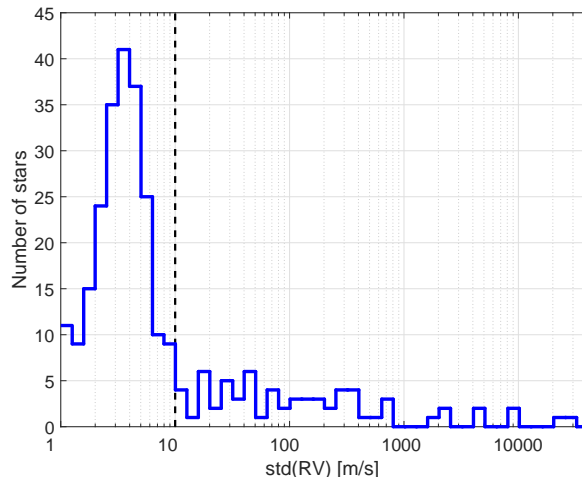

Fig. 1. Histogram of std(RV) per star of the 287 stars that were observed at least five times before September 2017. The RVs used for this plot were derived from the CARMENES VIS spectra with SERVAL (Zechmeister et al. 2018). The dashed line is the adopted boundary between RV-quiet and RV-loud stars at std(RV) = 10 m s^{-1}.

3. RV and activity measurements

All raw frames collected for the CARMENES survey are extracted and wavelength-calibrated with CARACAL, the CARMENES data-reduction pipeline (e.g., Caballero et al. 2016b). The CARACAL extraction procedure is based mainly on the REDUCE package (Piskunov & Valenti 2002) and on the flat-relative optimal-extraction algorithm (Zechmeister et al. 2014). Nightly wavelength calibrations are based on the spectra of three different hollow-cathode lamps: Th–Ne, U–Ne, and U–Ar (e.g., Lovis & Pepe 2007; Redman et al. 2011; Sarmiento et al. 2014; Ammler-von Eiff & Guenther 2017), and on a Fabry-Pérot etalon spectrum (Schäfer & Reiners 2012). Calibration spectra are taken at the beginning and end of each night. The wavemap for each night, that is, the wavelength value assigned to each pixel of the extracted frames of that night, is produced using the method described by (Bauer et al. 2015). The sub-pixel continuous drifts of both instrument channels are monitored by taking Fabry-Pérot etalon spectra simultaneously with stellar spectra through the additional fibers available in both channels (Quirrenbach et al. 2016).

3.1. RV measurements

Radial velocities are measured from the CARMENES spectra with SERVAL (Zechmeister et al. 2018), which is an iterative least-squares fitting algorithm similar to TERRA (Anglada-Escudé & Butler 2012). For each star SERVAL creates a template spectrum to fit its individual observations by coadding all CARMENES spectra of that star. Then SERVAL measures individual RVs for each echelle order, and the final RV for each observation is taken as the weighted average of the individual-order RVs.

We currently require a minimum of five spectra to produce a template spectrum for a given star and to calculate its RVs. By September 2017, all 324 CARMENES-sample stars were observed at least once (Reiners et al. 2018b), but only 287 of them fulfilled the $n_{\rm RV} \geq 5$ criterion.

Beyond true RV excursions caused by stellar orbital motions, there are several additional sources of RV scatter. First,

RV-measurement precision is limited by photon noise and by the amount of RV information in the observed stellar spectrum (e.g., Bouchy et al. 2001; Reiners et al. 2010). Second, instrumental systematic effects might cause sub-pixel shifts of the spectra that look similar to Doppler shifts. Not all systematic effects can be calibrated out (e.g., Halverson et al. 2016). Third, stellar activity can cause apparent RV signals, as discussed above.

Reiners et al. (2018b) showed that an RV precision of $\lesssim 1\,\mathrm{m\,s^{-1}}$ can be achieved in the VIS for CARMENES-sample stars with $v \sin i \lesssim 2\,\mathrm{km\,s^{-1}}$, except for a few faint and very late-type M dwarfs (M8.0–9.5 V). The median internal RV uncertainty that we measured from the VIS spectra taken before September 2017 was $\sim 1.3\,\mathrm{m\,s^{-1}}$. The deviation from $\sim 1.0\,\mathrm{m\,s^{-1}}$ can be explained by the fact that the survey includes 75 stars with $v \sin i > 2\,\mathrm{km\,s^{-1}}$ and some faint M8.0–9.5 V stars.

Trifonov et al. (2018) investigated the VIS RV accuracy of seven CARMENES-sample stars with known planetary systems, and the possible existence of systematic effects. They showed that despite our careful wavelength-calibration and drift-correction processes, which were shown to be precise at $<1\,\mathrm{m\,s^{-1}}$ level (Bauer et al. 2015), the measured RVs still contain nightly zero-point offsets (NZPs) at $\sim 3\,\mathrm{m\,s^{-1}}$ level. The origin of these NZPs is still being investigated. Nevertheless, when the RVs are corrected for the NZPs, the instrument performance is comparable to other PRV instruments, such as HARPS (Mayor et al. 2003) and HIRES (Vogt et al. 1994). Since the NZP uncertainties, which are added in quadrature to the internal RV uncertainties, are typically $\sim 1.0\,\mathrm{m\,s^{-1}}$, the median NZP-corrected RV uncertainty that we measured was $\sim 1.7\,\mathrm{m\,s^{-1}}$.

Figure 1 shows a histogram of RV standard-deviation values, std(RV), of the stars that were observed at least five times before September 2017. To avoid possible biases from outliers and small-number statistics, we estimated std(RV) as 1.48 times the median absolute deviation around the median (e.g., Rousseeuw & Croux 1993). The distribution peaks at 3–4 m s^{-1}, with tails extending out to $\sim 1\,\mathrm{m\,s^{-1}}$ and $\sim 10\,\mathrm{m\,s^{-1}}$. Hence, the RV scatter is larger than the typical uncertainties for most of the survey stars. This excess RV scatter can be explained by the presence of activity-induced RV variations and by reflex orbital motions caused by companion objects.

We here focus on the stars with std(RV) greater than $10\,\mathrm{m\,s^{-1}}$. We name them "RV-loud stars", and by September 2017, we had identified 67 such stars in the CARMENES sample. We expect the scatter of the RV-loud stars to be dominated by stellar activity and by possible orbital motions, but not by systematic measurement errors.

3.2. Rotation and activity measurements

Stellar rotation of M dwarfs, the amount and nature of active regions on their photospheres, and the level of chromospheric emission are three quantities that are closely related to each other (e.g., Reiners & Basri 2007). In order to estimate their impact on strong RV variability, we need to measure each of them independently.

Using CARMENES spectra, Reiners et al. (2018b) derived $v \sin i$ values for 75 out of the 324 CARMENES-sample stars. Given the instrument resolution (94,600 in the VIS), reliable values could only be derived for stars with $v \sin i \geq 2\,\mathrm{km\,s^{-1}}$. For the rest of the stars the value $v \sin i = 2\,\mathrm{km\,s^{-1}}$ can be used as an upper limit. Another independent measure of rotation is P_{rot}, which is usually determined from photometric time series. Unfortunately, we do not have P_{rot} values for many of the CARMENES-sample stars, including some of the fast rotators

(Caballero et al. 2016a; Díez Alonso et al. 2017; Reiners et al. 2018b; Jeffers et al. 2018).

Two indicators that may be related to photospheric activity levels were defined by Zechmeister et al. (2018) and are measured by SERVAL from each spectrum: the chromatic index (CRX) and the differential line width (dLW). The CRX is a measure of the RV–$\log \lambda$ correlation. For each observation, SERVAL fits a straight line to the scatter plot of its individual-order RVs vs $\log \lambda$. The slope of this line is defined as the CRX. The dLW indicates differential changes in the line widths of the observation compared to the template. Unfortunately, these two indicators are not direct measures of the spot-coverage fraction or the average spot-to-photosphere temperature contrast. However, for the wavelength range covered by CARMENES VIS, both Reiners et al. (2010) and Barnes et al. (2011) predicted a strong RV chromaticity to be created by cool spots on the surface of rotating M dwarfs, particularly for low spot-to-photosphere temperature contrast (e.g., $\sim 200\,\mathrm{K}$). In addition, Zechmeister et al. (2018) showed that dLW variations are correlated with the rotational phase of the active star YZ CMi.

Additional indicators of photospheric activity that we measure from CARMENES spectra are variations in the different CCF moments: the full width at half-maximum (FWHM), bisector inverse slope (BIS), and CCF contrast (e.g., Reiners et al. 2018a). Such variations can be related to changes in the distribution of inhomogeneities on the stellar surface (e.g., Herrero et al. 2016). Since M-dwarf visible-light spectra contain a large number of blended molecular lines (e.g., Reiners et al. 2018b), their CCF analysis is not as straightforward as it is for solar-type stars (e.g., Astudillo-Defru et al. 2015; Suárez Mascareño et al. 2017a). The situation is even more complicated for fast-rotating M dwarfs. We are currently extending our CCF analysis of M-dwarf spectra to also include fast rotators.

Several indicators of chromospheric activity are routinely measured from each CARMENES spectrum (e.g., Jeffers et al. 2018). They include measurements of excess emission in Hα, Na D$_1$ and D$_2$, and the Ca II infrared triplet, among other lines. The measurements are carried out by estimating the pseudo-equivalent width (pEW) of each line after subtracting from the observed star spectrum a template spectrum of an inactive star of a similar SpT. For instance, the pEW(Hα) values are measured in the wavelength region [6559.6, 6569.6 Å], after normalizing it in the regions [6550.0, 6555.0 Å] and [6576.0, 6581.0 Å]. This is similar to the methods described by Young et al. (1989) and Montes et al. (1995). We also translate pEW(Hα) measurements into Hα luminosity relative to the bolometric one ($\log L_{\mathrm{H}\alpha}/L_{\mathrm{bol}}$) using the relation

$$\frac{L_{\mathrm{H}\alpha}}{L_{\mathrm{bol}}} = -\mathrm{pEW}(\mathrm{H}\alpha) \cdot \chi(T_{\mathrm{eff}}), \tag{1}$$

where T_{eff} is the effective temperature of the star, which is estimated by translating its SpT to T_{eff} with the relations of Pecaut & Mamajek (2013). The χ values are taken from Reiners & Basri (2008). The SpT and an average $\log L_{\mathrm{H}\alpha}/L_{\mathrm{bol}}$ value for each CARMENES-sample star can be found in Reiners et al. (2018b).

For the purpose of investigating RV–rotation and RV–activity correlations in this paper, we focus on the following four quantities: $v \sin i$, CRX, dLW, and $\log L_{\mathrm{H}\alpha}/L_{\mathrm{bol}}$. We do not use P_{rot} as a measure of rotation, not only because we do not have it for all of our stars, but also because we wish to limit ourselves to quantities that can be determined directly from the spectra. We use only $\log L_{\mathrm{H}\alpha}/L_{\mathrm{bol}}$ as a chromospheric-activity indicator, both because Hα is the line that is most widely used for that purpose

(e.g. Jeffers et al. 2018) and because our preliminary results show that the variations in chromospheric emission can be measured more accurately in Hα than in the other lines.

4. CARMENES sample of active RV-loud stars

The goal of this paper is to study the main common features of activity-induced RV variations on a sample of stars, rather than making an in-depth analysis of individual active stars. To do so, we selected a subsample of stars for which we could attribute the RV scatter to rotation and/or activity with high confidence. Only stars that fulfilled the following criteria were selected for the study:

– no orbital RV variations of $>10\,\mathrm{m\,s^{-1}}$ due to companions, either known or suspected;
– std(RV) $> 10\,\mathrm{m\,s^{-1}}$;
– number of RVs per star $n_{RV} > 10$;
– $v\sin i > 2\,\mathrm{km\,s^{-1}}$.

The reasoning behind these criteria is detailed below.

First, we removed from the sample 17 RV-loud stars whose RV scatter is dominated by orbital motion and not by stellar activity: 4 known planetary systems (Trifonov et al. 2018), and another 13 spectroscopic binaries that passed our initial survey filters (e.g., Cortés-Contreras et al. 2017; Jeffers et al. 2018), but were discovered at an early stage of the CARMENES survey. Most of the new binaries have std(RV) $> 1\,\mathrm{km\,s^{-1}}$, and they will be addressed in a forthcoming paper.

Next, we excluded the 220 RV-quiet stars with std(RV)$< 10\,\mathrm{m\,s^{-1}}$ because separating orbital RV signals from activity-induced ones close to the measurement accuracy limit with a small number of RVs is a difficult task. With $\mathrm{m\,s^{-1}}$ instruments, the separation of signals smaller than $10\,\mathrm{m\,s^{-1}}$ typically relies on periodogram analysis, comparing significant RV frequencies with significant frequencies of the different activity indicators (e.g., Bonfils et al. 2007; Suárez Mascareño et al. 2017b). However, for a small number of data points and a low RV-scatter to RV-uncertainty ratio, there is a low probability of finding any significant periodogram peaks (e.g., Zechmeister & Kürster 2009). With a median number of 11 RVs per star and a median RV uncertainty of $\sim 1.7\,\mathrm{m\,s^{-1}}$, we decided to exclude from our analysis here all RV-quiet stars. We postpone the investigation of their activity-induced RV signals to after we have acquired enough RVs per star to compute and analyze meaningful periodograms.

The std(RV) of the remaining 50 RV-loud stars ranges from 0.01 to 2.0 $\mathrm{km\,s^{-1}}$. Thus, these stars represent the high end of the expected activity-induced RV scatter in M dwarfs (e.g., Barnes et al. 2011). However, even with a high ratio of the RV-scatter to RV-uncertainty, our experience shows that it is hard to distinguish between orbital and activity-induced RV signals for $n_{RV} \leq 10$. With such a low n_{RV}, it is possible to confirm the compatibility of the RV variations with a known period (e.g., Tal-Or et al. 2015), but it is impossible to reliably determine the parameters of a signal of an unknown period (e.g., Halbwachs et al. 2014). For that reason, we excluded another 14 RV-loud stars with $n_{RV} \leq 10$, and left them for future analysis.

Applying the criteria above in a different order, we selected the remaining 36 RV-loud stars from the 166 stars that were observed at least 11 times by September 2017. Using the published occurrence rates of planets around M dwarfs (Fressin et al. 2013; Dressing & Charbonneau 2013), Garcia-Piquer et al. (2017) estimated the exoplanet yield of the CARMENES survey.
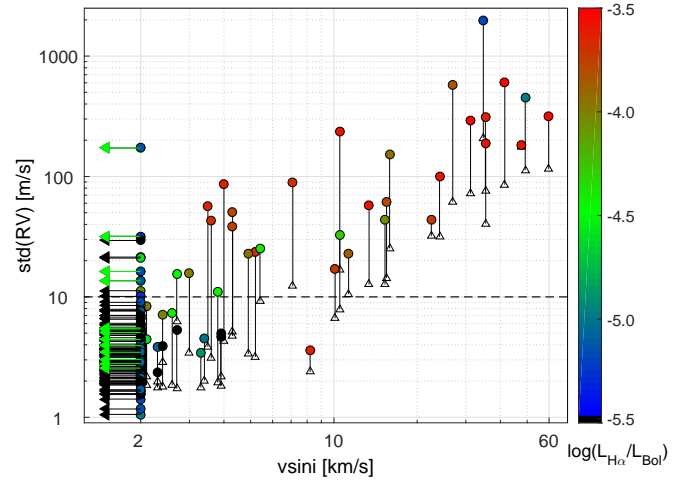

Fig. 2. CARMENES VIS std(RV)–$v\sin i$ scatter plot for the 166 stars with $n_{RV} > 10$. The points are color-coded according to their Hα luminosity. Stars with only an upper limit of $v\sin i \lesssim 2\,\mathrm{km\,s^{-1}}$ are marked with arrows: green arrows for host stars of known planetary systems, and black arrows for stars with no detected planets. The open triangles are the median RV uncertainties ($\overline{\delta RV}$) of the stars with $v\sin i > 2\,\mathrm{km\,s^{-1}}$. For clarity, each triangle is connected by a solid line to its point. The dashed line is the adopted boundary between RV-quiet and RV-loud stars at std(RV) = $10\,\mathrm{m\,s^{-1}}$.

They concluded that the largest RV semi-amplitudes that will be discovered by CARMENES should be $\sim 30\,\mathrm{m\,s^{-1}}$, and that the CARMENES sample should include ~ 10 planets that exert RV semi-amplitudes of 10–$30\,\mathrm{m\,s^{-1}}$ on their hosts. Hence, a handful of such systems could be contained in this subsample of 166 stars with $n_{RV} > 10$.

Figure 2 presents the std(RV)–$v\sin i$ scatter plot of these 166 stars. The points are color-coded according to their Hα luminosity. In addition, hosts of known planetary systems are marked with green arrows. Above the $10\,\mathrm{m\,s^{-1}}$ boundary, which we adopted to separate RV-quiet from RV-loud stars, stars with $v\sin i$ values above and below $2\,\mathrm{km\,s^{-1}}$ seem to form two distinct groups. While the stars with $v\sin i > 2\,\mathrm{km\,s^{-1}}$ typically have strong Hα emission and no known planets, the group of stars with $v\sin i \lesssim 2\,\mathrm{km\,s^{-1}}$ have weaker Hα emission and a few known planets. If planetary occurrence rates are not sensitive to $v\sin i$ values, we expect most of the stars with orbital RV semi-amplitudes of 10–$30\,\mathrm{m\,s^{-1}}$ to have $v\sin i \lesssim 2\,\mathrm{km\,s^{-1}}$, and that only one or two of these stars will have $v\sin i > 2\,\mathrm{km\,s^{-1}}$. Therefore, to minimize the chances of including in the selected sample stars whose RV scatter is dominated by planets as yet undiscovered, we excluded the five stars with std(RV) of 10–$30\,\mathrm{m\,s^{-1}}$ but $v\sin i \lesssim 2\,\mathrm{km\,s^{-1}}$. The RV scatter of some of these stars could still be dominated by activity, but to be extra careful, we leave this question for future analysis.

We are thus left with 31 stars, which we name the "CARMENES sample of active RV-loud stars". We do not claim that these stars do not have planetary systems, but that most likely the RV scatter of these stars is dominated by activity rather than by orbital motions. We find this sufficient to use this sample for investigating the main features of activity-induced RVs.

Table 1 lists the main properties of our active RV-loud stars. Their SpT distribution shows that most of the stars in the sample (24/31) are mid-type M dwarfs (M3.0–5.5 V). There are only two early-type M dwarfs (M0.0–2.5 V), and only five late-type M dwarfs (M6.0–9.0 V) in the sample. However, the fraction of active RV-loud stars in the whole CARMENES sample increases

Table 1. Main properties of the active RV-loud sample.

Karmn	Name	α (J2000)	δ (J2000)	J (mag)	SpT	$P_{\rm rot}$ (d)	$v \sin i$ (km s^{-1})	$\log L_{{\rm H}\alpha}/L_{\rm bol}$
J01033+623	V388 Cas	01:03:21.49	+62:21:57.2	8.61	M5.0 V	1.06	10.5	−3.57
J01352−072	Barta 161 12	01:35:14.05	−07:12:52.8	8.96	M4.0 V	...	59.8	−3.50
J02088+494	G 173-039	02:08:54.00	+49:26:52.0	8.42	M3.5 V	...	24.1	−3.56
J03473−019	G 080-021	03:47:23.54	−01:58:24.1	7.80	M3.0 V	3.88	5.2	−3.69
J04472+206	RX J0447.2+2038	04:47:12.35	+20:38:09.3	9.38	M5.0 V	...	47.6	−3.55
J05365+113	V2689 Ori	05:36:30.98	+11:19:39.2	6.13	M0.0 V	12.04	3.8	−4.45
J06000+027	G 099-049	06:00:03.86	+02:42:22.9	6.91	M4.0 V	1.81	4.9	−3.93
J07446+035	YZ CMi	07:44:39.79	+03:33:01.4	6.58	M4.5 V	2.78	4.0	−3.62
J08298+267	DX Cnc	08:29:48.11	+26:46:24.5	8.23	M6.5 V	0.46	10.5	−4.31
J09449−123	G 161-071	09:44:53.84	−12:20:53.8	8.50	M5.0 V	...	31.2	−3.37
J12156+526	StKM 2-809	12:15:39.56	+52:39:08.9	8.59	M4.0 V	...	35.3	−3.64
J12189+111	GL Vir	12:18:57.94	+11:07:37.3	8.53	M5.0 V	0.49	15.5	−3.79
J14173+454	RX J1417.3+4525	14:17:22.17	+45:25:45.7	9.47	M5.0 V	...	15.9	−3.94
J15218+209	OT Ser	15:21:53.01	+20:58:41.7	6.61	M1.5 V	3.38	4.3	−3.75
J15499+796	LP 022-420	15:49:53.86	+79:39:53.9	9.72	M5.0 V	...	26.9	−3.83
J16313+408	G 180-060	16:31:18.57	+40:51:56.8	9.46	M5.0 V	0.51	7.1	−3.68
J16555−083	vB 8	16:55:34.36	−08:23:54.8	9.78	M7.0 V	...	5.4	−4.40
J16570−043	LP 686-027	16:57:06.24	−04:21:02.3	7.97	M3.5 V	1.21	10.1	−3.71
J17338+169	1RXS J173353.5+165515	17:33:53.02	+16:55:10.7	8.89	M5.5 V	0.27	41.5	−3.51
J18022+642	LP 071-082	18:02:17.11	+64:15:38.1	8.54	M5.0 V	0.28	11.3	−3.86
J18189+661	LP 071-165	18:18:58.45	+66:11:25.6	8.74	M4.5 V	...	15.3	−4.07
J18356+329	LSR J1835+3259	18:35:37.80	+32:59:41.6	10.27	M8.5 V	...	49.2	−5.01
J18498−238	V1216 Sgr	18:49:50.08	−23:50:13.3	6.22	M3.5 V	2.87	3.0	−4.01
J19169+051S	V1298 Aql (vB 10)	19:16:56.97	+05:08:39.8	9.91	M8.0 V	...	2.7	−4.51
J19255+096	LSPM J1925+0938	19:25:30.99	+09:38:19.3	11.21	M8.0 V	...	34.7	−5.25
J19511+464	G 208-042	19:51:09.61	+46:29:04.5	8.59	M4.0 V	0.59	22.5	−3.72
J20093−012	2M J20091824-0113377	20:09:18.18	−01:13:44.1	9.40	M5.0 V	...	4.3	−3.77
J22012+283	V374 Peg	22:01:13.59	+28:18:25.5	7.63	M4.0 V	0.45	35.4	−3.57
J22468+443	EV Lac	22:46:48.71	+44:19:55.4	6.11	M3.5 V	4.38	3.5	−3.65
J22518+317	GT Peg	22:51:54.18	+31:45:14.4	7.70	M3.0 V	1.64	13.4	−3.55
J23548+385	RX J2354.8+3831	23:54:51.27	+38:31:34.8	8.94	M4.0 V	4.76	3.6	−3.68

Notes. Values are taken from Carmencita and Reiners et al. (2018b).

monotonically with SpT. In the subsample of 166 stars with $n_{\rm RV} > 10$, the fractions of early-, mid-, and late-type active RV-loud stars are 2/70 (3%), 24/88 (27%), and 5/8 (63%), respectively.

5. Observed connection between RV scatter, stellar rotation, and stellar activity

5.1. Correlations of std(RV) with global spectral parameters

Table 2 shows the $n_{\rm RV}$ and std(RV) values, as well as the median RV uncertainties ($\overline{\delta {\rm RV}}$), of the active RV-loud stars, which were measured from their CARMENES VIS spectra. As a measure of std(RV) uncertainty we took std(RV)$(2\,n_{\rm RV})^{-0.5}$ (Press et al. 2002).

To understand the mechanisms driving the observed large RV scatter, we first searched for correlations between std(RV) and three of the parameters shown in Table 1: SpT, $v \sin i$, and $\log L_{{\rm H}\alpha}/L_{\rm bol}$. These three parameters were chosen because they were previously suggested to influence the RV-scatter amplitude (e.g., Barnes et al. 2011). Unfortunately, we do not have indicators of the photospheric level of activity, from which we could estimate the spot-coverage fraction, or the average

spot-to-photosphere temperature contrast. The chromospheric Hα emission can be used as a proxy to the photospheric activity level only if the two are correlated – a non-trivial assumption for M dwarfs (e.g., Reiners & Basri 2007, 2010).

To estimate linear correlation significance, we used the p(F$_{\rm test}$) value (Fisher 1925) of fitting a straight line to the data. The default p-value threshold frequently used for claiming a statistically significant correlation is 0.05 (or log(p-value) = −1.3). Recently, Benjamin et al. (2018) proposed that it should be redefined to 0.005 (log(p-value) = −2.3), and that findings with 0.005 < p-value < 0.05 should be labeled as having "suggestive evidence". We follow these criteria.

Figure 3 shows the std(RV)–$v \sin i$, std(RV)–SpT, and std(RV)–$\log L_{{\rm H}\alpha}/L_{\rm bol}$ correlation plots. The points are color-coded according to SpT. In each plot we estimated two linear correlation significances: one for the whole active RV-loud sample (31 stars), and one for the subsample of mid-type M dwarfs (24 stars). To prevent the difference in sample size from affecting the p-values, we bootstrapped the sample with 1000 iterations, selecting each time a random subsample of 21 stars for the p-value estimation. The final p-values were taken as the medians of these 1000 iterations, and the p-value uncertainties were tuned to cover the central 68.2% of the distribution. The resulting p-values are shown in the plot insets.

Table 2. CARMENES VIS results for the active RV-loud sample.

Karmn	Name	n_{RV}	$\overline{\delta RV}$ (m s^{-1})	std(RV) (m s^{-1})	RV–CRX log(p-value)	RV–dLW log(p-value)	RV–log $L_{H\alpha}/L_{bol}$ log(p-value)
J01033+623	V388 Cas	12	16.8	237 ± 48	−5.6	−0.4	−0.4
J01352-072	Barta 161 12	11	115.6	315 ± 67	−2.8	−1.1	−2.2
J02088+494	G 173-039	17	31.5	100 ± 17	−0.3	−0.5	−0.1
J03473-019	G 080-021	11	3.2	24 ± 5	−0.1	−1.0	−0.4
J04472+206	RX J0447.2+2038	11	177.1	182 ± 39	−0.1	−0.1	−0.3
J05365+113	V2689 Ori	31	1.9	11 ± 1	−0.3	−1.2	−1.9
J06000+027	G 099-049	14	3.4	23 ± 4	−2.7	−0.2	−0.4
J07446+035	YZ CMi	44	4.3	87 ± 9	−13.8	−0.2	−0.3
J08298+267	DX Cnc	13	7.9	33 ± 6	−0.6	−0.3	−0.1
J09449-123	G 161-071	11	72.0	290 ± 62	−0.7	−0.7	−0.6
J12156+526	StKM 2-809	12	75.6	314 ± 64	−1.8	−0.9	−0.2
J12189+111	GL Vir	12	14.4	61 ± 13	−1.8	−0.1	−0.1
J14173+454	RX J1417.3+4525	12	25.3	152 ± 31	−0.4	−0.4	−1.4
J15218+209	OT Ser	36	5.2	39 ± 5	−6.0	−0.2	−0.3
J15499+796	LP 022-420	14	61.6	577 ± 109	−0.3	−0.3	−1.4
J16313+408	G 180-060	12	12.3	89 ± 18	−1.7	−0.3	−0.3
J16555-083	vB 8	104	9.2	25 ± 2	−0.8	−0.7	−0.8
J16570-043	LP 686-027	13	6.7	17 ± 3	−0.1	−0.6	−0.5
J17338+169	1RXS J173353.5+165515	12	85.3	604 ± 123	−1.5	−0.6	−0.3
J18022+642	LP 071-082	14	10.5	23 ± 4	−0.8	−0.3	−0.3
J18189+661	LP 071-165	12	12.7	44 ± 9	−1.7	−0.2	−0.2
J18356+329	LSR J1835+3259	14	112.9	449 ± 85	−2.7	−2.8	−0.3
J18498-238	V1216 Sgr	25	3.4	16 ± 2	−0.6	−0.3	−0.0
J19169+051S	V1298 Aql (vB 10)	31	6.3	16 ± 2	−1.3	−0.2	−0.4
J19255+096	LSPM J1925+0938	15	208.1	1986 ± 363	−6.9	−0.5	−0.7
J19511+464	G 208-042	13	32.0	44 ± 9	−1.1	−0.1	−0.1
J20093-012	2M J20091824-0113377	12	4.7	51 ± 10	−5.0	−0.5	−0.7
J22012+283	V374 Peg	12	40.6	190 ± 39	−0.6	−0.0	−0.0
J22468+443	EV Lac	74	3.8	57 ± 5	−16.0	−0.0	−0.5
J22518+317	GT Peg	12	12.7	58 ± 12	−1.5	−0.0	−0.0
J23548+385	RX J2354.8+3831	13	3.1	43 ± 8	−5.1	−0.6	−0.1
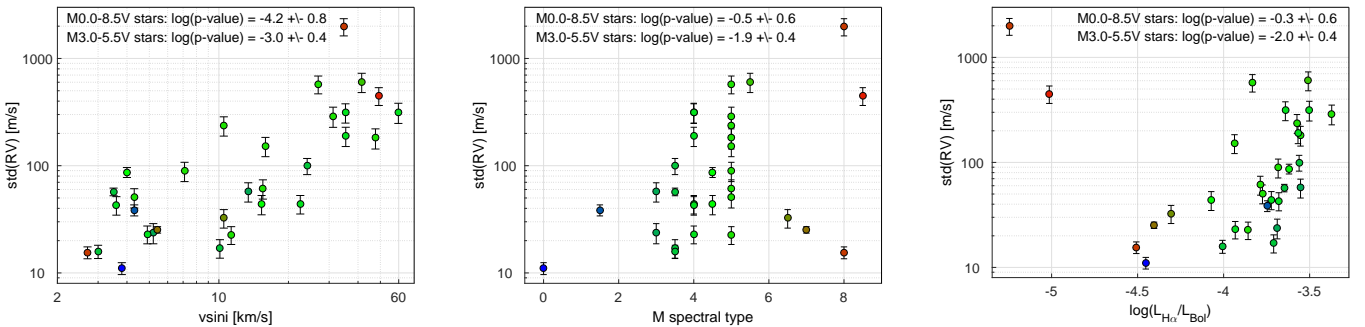
Fig. 3. Correlating std(RV) of the active RV-loud stars with three of their spectral parameters – *left*: $v \sin i$; *middle*: SpT; and *right*: log $L_{H\alpha}/L_{bol}$. The points are color-coded according to SpT in all three plots, from M0 in blue to M9 in red. Correlation significances, as measured by the p(F_{test}) values, are shown in the insets. A log(p-value) < -2.3 means a significant correlation, while a log(p-value) between -1.3 and -2.3 means a marginal correlation.

There is a significant std(RV)–$v \sin i$ correlation in our active RV-loud sample. There are no std(RV)–log $L_{H\alpha}/L_{bol}$ or std(RV)–SpT correlations for the whole sample, but there is suggestive evidence for such correlations when we restrict our sample to only the mid-type M dwarfs.

The std(RV)–$v \sin i$ correlation suggests that the spectral line broadening that accompanies stellar rotation plays an important role in driving strong RV scatter in active M dwarfs. In order to verify that the loss of RV information content due to the spectral line broadening is not, by itself, sufficient to explain the observed RV scatter and that it is the combination of activity and rotation that drives it, we performed the following test: we repeated the correlation analysis shown in Fig. 3 after replacing the std(RV) values with the excess RV scatter of each star, which we defined as the quadratic difference (std(RV)$^2 - \overline{\delta RV}^2)^{0.5}$. We found this substitution to slightly

weaken the correlation significances presented in Fig. 3, but not to change the presented qualitative results. For instance, the log(p-value) of the linear correlation between excess RV scatter and $v \sin i$ for the full sample of active RV-loud stars was found to be -3.3. This indicates a weaker correlation than the std(RV)–$v \sin i$ one, for which we found log(p-value) = -4.2, but it is still significant.

The marginal std(RV)–log $L_{H\alpha}/L_{bol}$ correlation for the mid-type M dwarfs could be explained in three ways: (1) a higher chromospheric emission directly drives a higher RV scatter; (2) the level of chromospheric emission is correlated with the level of photospheric activity, but the spots are the ones that drive RV scatter; and (3) this correlation is an indirect outcome of the std(RV)–$v \sin i$ correlation, and the rotation-activity correlation for M dwarfs (e.g., Reiners & Basri 2007; Newton et al. 2017; Jeffers et al. 2018). The last explanation could also hold true for the weak std(RV)–SpT correlation seen for the mid-type M dwarfs in Fig. 3, which could be an indirect outcome of the rotation-SpT correlation in this range of spectral types (e.g., Reiners et al. 2012).

The above findings are in agreement with the predictions of Reiners et al. (2010) and Barnes et al. (2011). Their simulations suggest that the large scatter around the std(RV)–$v \sin i$ correlation seen in the left panel of Fig. 3 could be caused by the spot characteristics of the active stars, such as their spot coverage fraction, and their spot-to-photosphere temperature contrast. We also recall that an additional source of scatter could be true orbital motions of these stars due to their as yet undiscovered planetary systems.

5.2. Correlations of RVs with spectral activity indicators

After searching for correlations between std(RV) and activity-related stellar parameters of the active RV-loud sample as a whole, we moved on to investigate individual stars of the sample for correlations between their stellar activity indicators and their measured RVs. Finding a parametric function that could translate measurable spectral activity indicators into RV deviations is a great challenge, but at the same time, it holds the promise to enable the modeling of RV time series with a combined model of planetary- and activity-induced signals. Moreover, such a function would obviate simultaneous auxiliary measurements to quantify activity-induced RVs, such as multi-band photometric observations. Unfortunately, no such a function has been proposed so far for M dwarfs. Lacking a physical model to guide our spectral data exploration, we searched our active RV-loud stars for linear correlations between their varying RVs and three of the spectral activity indicators that we have chosen to investigate in this paper: CRX, dLW, and log $L_{H\alpha}/L_{bol}$.

To best illustrate the process, we show here a few representative plots for one of the most frequently observed stars in our sample: J22468+443 (EV Lac). In order to demonstrate the CRX definition, we show in the top panel of Fig. 4 the order-by-order RVs from four representative observations of EV Lac: three observations with close-to-median Hα emission but different CRX values, and one observation with extremely high Hα emission. The latter observation was taken during a strong flare event (Fuhrmeister et al. 2018). The slopes of the best-fit lines to these RV–order scatter plots are related to the CRX values of these four observations (Zechmeister et al. 2018). The locations of activity-induced emission lines are marked at the top panel of Fig. 4. The bottom panel of Fig. 4 shows the corresponding CARMENES spectra from these four observations, centered on the Hα line.
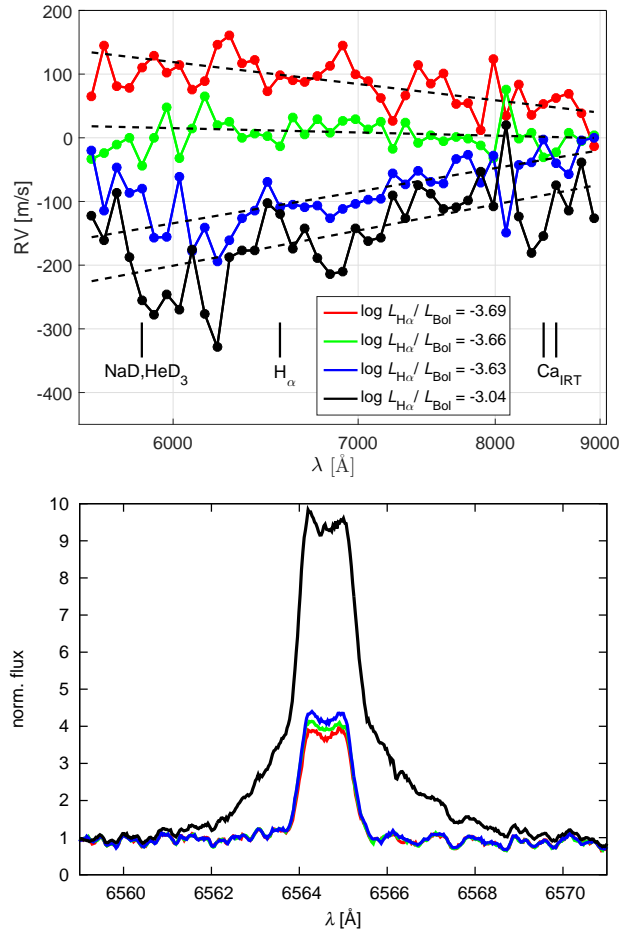
Fig. 4. CARMENES VIS measurements of J22468+443 (EV Lac). *Top*: Order-by-order RVs from four representative observations. Red, green, and blue show three observations with close-to-median Hα emission. Black plots an observation with extremely high Hα emission, taken during a strong flare event (Fuhrmeister et al. 2018). The corresponding log $L_{H\alpha}/L_{bol}$ values are given in the inset. Dashed lines show the best-fit straight lines to the RV–order scatter plots of each observation. Individual-order RV uncertainties are not shown in the plot for clarity, but they are on the order of $10–30\,\mathrm{m\,s^{-1}}$, depending on the RV-information content and the S/N in each order. The markers at the bottom specify the locations of the indicated chromospheric emission lines. *Bottom*: Parts of the VIS spectra from these four observations, centered on the Hα line. The colors are the same as in the top panel.

The upper panel of Fig. 4 shows that the RVs of EV Lac are strongly wavelength dependent. This dependence could be fit by a linear RV–log λ relation in virtually all observations, which means significant CRX values. The observation made during the strong flare event (black lines in Fig. 4) also showed a linear RV–log λ dependence, but its median RV was lower by $\sim$50 m s^{-1} from an observation with a similar CRX value, but a normal Hα emission (blue lines in Fig. 4). Hence, the flare affects all order RVs in a similar fashion, introducing a similar deviation in all orders.

Figure 5 shows the RV–CRX, RV–dLW, and RV–log $L_{H\alpha}/L_{bol}$ scatter plots for EV Lac. Similar scatter plots for the other 30 active RV-loud stars are presented in Fig. A.1. As with the correlations between std(RV) and global stellar parameters, we again used the p(F_{test}) values of the best-fit lines to these scatter plots to estimate the RV–CRX, RV–dLW, and RV–log $L_{H\alpha}/L_{bol}$ linear-correlation significances for all 31 active RV-loud stars. The calculated p-values are listed in Table 2.
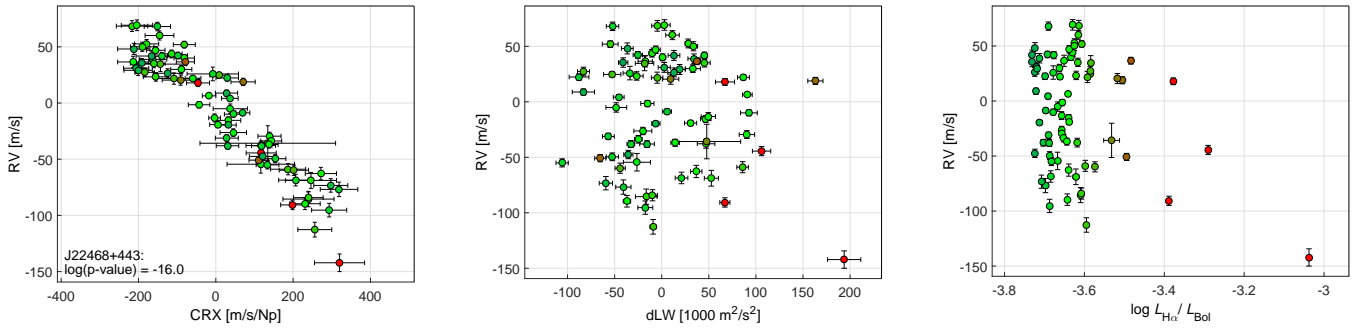
Fig. 5. CARMENES VIS measurements of EV Lac. RV–CRX (*left*), RV–dLW (*middle*), and RV–log $L_{H\alpha}/L_{bol}$ (*right*) scatter plots. Points are color-coded according to their log $L_{H\alpha}/L_{bol}$ value, with Hα enhancement of >0.25 dex colored red. The CARMENES star id (Karmn) and the log(p-value) of the linear RV–CRX correlation are shown in the left panel. At least eight epochs of enhanced chromospheric activity can be seen via their higher Hα emission, with the highest one belonging to a strong flare event. The outliers at the bottom of the left and middle panels belong to this event (see Fig. 4 for its Hα profile).
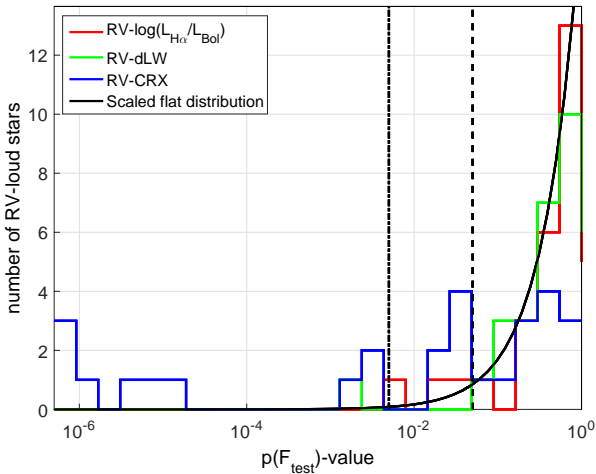
Fig. 6. Histograms of p(F$_{test}$) values of fitting a straight line to the RV–CRX, RV–dLW, and RV–log $L_{H\alpha}/L_{bol}$ scatter plots for the stars in Table 1. The solid black curve represents a uniform distribution between 0 and 1 scaled so that its integral is equal the number of RV-loud stars. The dashed vertical line is the critical p-value for suggestive evidence (0.05), and the dash-dotted vertical line is the critical p-value for significant evidence (0.005). The histogram is truncated at 5×10^{-7}. Lower p-values are contained in the left-most column.

For EV Lac, there is a strong linear RV–CRX anticorrelation, while there are no RV–dLW or RV–log $L_{H\alpha}/L_{bol}$ correlations. The RV–CRX anticorrelation, also referred to as a negative chromaticity (Zechmeister et al. 2018), indicates that the RV scatter decreases toward longer wavelength. This can also be seen in Fig. 4. This behavior is in agreement with the predictions of Reiners et al. (2010) and Barnes et al. (2011) for a relatively low spot-to-photosphere temperature contrast.

Figure 6 shows the RV–CRX, RV–dLW, and RV–log $L_{H\alpha}/L_{bol}$ linear-correlation p-value distributions on a log scale. The three distributions are compared to a uniform distribution between 0 and 1, which is the expected p-value distribution for the case of no correlation between these pairs of parameters (e.g., Hung et al. 1997). The deviation of the RV–CRX p-value distribution from a uniform one indicates that these two quantities are correlated for a large fraction of our active RV-loud stars. Using the criteria of Benjamin et al. (2018), the RV–CRX correlation is significant for 10/31 stars, and marginal for another 7/31 stars. For comparison, the RV–dLW correlation

is significant for only one star (namely LSR J1835+3259), and there is a marginal RV–log $L_{H\alpha}/L_{bol}$ correlation for four stars only. Moreover, all 10 stars with a significant RV–CRX correlation have a negative chromaticity. These findings are in agreement with the predictions of Reiners et al. (2010) and Barnes et al. (2011). The lack of RV chromaticity in about half of our active RV-loud stars can be explained by one (or more) of the following:

– complex spot patterns, with multiple spots whose chromatic contribution nearly cancels out;
– higher spot-to-photosphere temperature contrasts;
– strong magnetic fields associated with their spots, which counteract the flux-contrast RV chromaticity via the Zeeman splitting effect (Reiners et al. 2013).

The lack of linear RV–log $L_{H\alpha}/L_{bol}$ or RV–dLW correlations does not exclude the possibility of more complicated relations. For instance, Bonfils et al. (2007) showed a "closed-loop" relation between RVs and Hα-index measurements of GJ 674. In addition, Zechmeister et al. (2018) showed for YZ CMi that the position of each data point in the RV–dLW plane could depend on the rotational phase. Such interesting relations should probably be tested with a larger sample of active stars with known P_{rot}. In addition, we should try reproducing such behavior with numeric simulations.

6. Summary and future work

During the first 20 months of the CARMENES survey, we observed all 324 CARMENES sample stars (Reiners et al. 2018b). From their VIS spectra, we derived precise RVs for the 287 stars that fulfilled the $n_{RV} \geq 5$ criterion (Zechmeister et al. 2018), with a median $\overline{\delta RV}$ of ~1.7 m s^{-1}. Similarly to previous PRV surveys of M dwarfs (e.g., Bonfils et al. 2013), we found the std(RV) distribution of the observed stars to peak at 3–4 m s^{-1}. Currently, one of the main challenges of the CARMENES consortium is to explain the excess RV scatter for each star with a well-established model comprised of orbital motion and stellar activity.

Among the 287 stars with $n_{RV} \geq 5$, we detected 67 stars with std(RV) of >10 m s^{-1}. Of these, we selected for the active RV-loud sample 31 stars that have $n_{RV} > 10$, $v \sin i > 2$ km s^{-1} and no known or suspected low-mass companions in orbit around them. This sample downsizing was done to ensure that the RV scatter of the stars in the sample is dominated by activity and not by orbital motion. Nevertheless, it is the largest and most

comprehensive sample of active RV-loud M dwarfs investigated to date with a PRV instrument. We found the fraction of active RV-loud stars to increase with spectral type: from ∼3% for early-type M dwarfs through ∼30% for mid-type M dwarfs to >50% for late-type M dwarfs. This finding is consistent with the increase in the fraction of fast-rotating and active M dwarfs with spectral type (e.g., Reiners et al. 2012; Jeffers et al. 2018).

While investigating the relations between std(RV) and other stellar parameters of the active RV-loud stars, we found significant evidence for a positive std(RV)–$v \sin i$ correlation in all M-dwarf spectral types. Suggestive evidence for positive std(RV)–$\log L_{H\alpha}/L_{bol}$ and std(RV)–SpT correlations was found only for the mid-type M dwarfs. In addition, we have shown that the spectral line broadening caused by the rapid rotation of these stars is not sufficient to explain the observed RV scatter, and that the excess RV scatter is most likely caused by the additional photospheric activity that accompanies the rapid rotation. Our findings are in agreement with predictions from numeric simulations (e.g., Reiners et al. 2010; Barnes et al. 2011).

Furthermore, we searched the active RV-loud sample for correlations between each star's RVs and three of its activity indicators: CRX, dLW, and $\log L_{H\alpha}/L_{bol}$. We found a significant RV–CRX correlation for ∼30% of the stars, and a marginal correlation for another ∼20% of them. For most of these stars we found a negative chromaticity, which means that the RV scatter decreases with wavelength. Comparing our findings with the predictions made by Reiners et al. (2010), Barnes et al. (2011), and Reiners et al. (2013), we see that such behavior can most likely be created by active regions on the surface of the rotating stars. The lack of RV chromaticity for about half of our active RV-loud sample can be explained by complex spot patterns, higher spot-to-photosphere temperature contrasts, or strong magnetic fields associated with their spots.

We found no significant linear RV–dLW or RV–$\log L_{H\alpha}/L_{bol}$ correlations for the vast majority of the active RV-loud sample. However, we did not exclude the possibility of more complicated relations between these two pairs of observables, such as the "closed-loop" relations that were found by Bonfils et al. (2007) and Zechmeister et al. (2018), for example.

Periodogram analyses could reveal common periods for the different activity indicators and RVs. For instance, Suárez Mascareño et al. (2017b) used such period matching to attribute to activity 1–10 m s^{-1} signals of 18 M dwarfs. Moreover, matching the periods with photometrically measured rotation periods (or their harmonics) can help distinguishing between planetary- and activity-induced RV signals. However, for an accurate derivation of orbital parameters from RV time series of active stars, period discrimination is not enough. For this, one would have to model the activity-induced signals together with the orbital solution. Revealing the exact relations between spectral activity indicators and RVs would greatly help in such modeling. Deepening the understanding of such relations is on the agenda of the CARMENES consortium.

To this end, we do not have a direct measure of the spot-coverage fraction, or the average spot-to-photosphere temperature contrast – two important parameters for understanding activity-induced RVs of M dwarfs (e.g., Barnes et al. 2011). We are working on identifying spectral indicators that will enable estimating these two quantities (e.g., Herrero et al. 2016). For example, finding a correlation between the different CCF moments and RV deviations of active stars would be an important step toward modeling activity-induced RVs.

In the coming few years, several novel instruments promise to push down RV-measurement precision towards 0.1–0.3 m s^{-1}

(e.g., Pepe et al. 2014; Halverson et al. 2016). Such precision would mean that activity-induced RV variations are expected to be larger than the RV uncertainties for most of the M dwarfs, most of the time. Under these circumstances, extending our picture of planetary occurrence rates to lower-mass planets and lower-mass stars will require a paradigm shift, from treating activity-induced RV variations as an additional noise source (e.g., Wright 2005) to modeling RV time series with both orbital- and activity-induced signals (e.g., Hébrard et al. 2016; Barnes et al. 2017). Farther in the future, one could even consider forward modeling the spectra themselves with the same ingredients.

References

Alonso-Floriano, F. J., Morales, J. C., Caballero, J. A., et al. 2015, A&A, 577, A128
Ammler-von Eiff, M., & Guenther, E. W. 2017, Astron. Nachr., 338, 550
Anglada-Escudé, G., & Butler, R. P. 2012, ApJS, 200, 15
Anglada-Escudé, G., Amado, P. J., Barnes, J., et al. 2016, Nature, 536, 437
Astudillo-Defru, N., Bonfils, X., Delfosse, X., et al. 2015, A&A, 575, A119
Barnes, J. R., Jeffers, S. V., & Jones, H. R. A. 2011, MNRAS, 412, 1599
Barnes, J. R., Jenkins, J. S., Jones, H. R. A., et al. 2014, MNRAS, 439, 3094
Barnes, J. R., Jeffers, S. V., Anglada-Escudé, G., et al. 2017, MNRAS, 466, 1733
Bauer, F. F., Zechmeister, M., & Reiners, A. 2015, A&A, 581, A117
Benjamin, D. J., Berger, J. O., Johannesson, M., et al. 2018, Nature Human Behaviour, 2, 6
Bonfils, X., Mayor, M., Delfosse, X., et al. 2007, A&A, 474, 293
Bonfils, X., Delfosse, X., Udry, S., et al. 2013, A&A, 549, A109
Bouchy, F., Pepe, F., & Queloz, D. 2001, A&A, 374, 733
Caballero, J. A., Cortés-Contreras, M., Alonso-Floriano, F. J., et al. 2016a, in 19th Cambridge Workshop on Cool Stars, Stellar Systems, and the Sun , 148
Caballero, J. A., Guàrdia, J., López del Fresno, M., et al. 2016b, in Observatory Operations: Strategies, Processes, and Systems VI, Proc. SPIE, 9910, 99100E
Campbell, B., Walker, G. A. H., & Yang, S. 1988, ApJ, 331, 902
Cortés-Contreras, M., Béjar, V. J. S., Caballero, J. A., et al. 2017, A&A, 597, A47
Dekker, H., D'Odorico, S., Kaufer, A., Delabre, B., & Kotzlowski, H. 2000, Optical and IR Telescope Instrumentation and Detectors, eds. M. Iye, & A. F. Moorwood, Proc. SPIE, 4008, 534
Díez Alonso, E., Montes, D., de Cos Juez, F. J., et al. 2017, in Highlights on Spanish Astrophysics IX, 502
Donati, J.-F., Forveille, T., Collier Cameron, A., et al. 2006, Science, 311, 633
Dressing, C. D., & Charbonneau, D. 2013, ApJ, 767, 95
Dumusque, X., Boisse, I., & Santos, N. C. 2014, ApJ, 796, 132
Fisher, R. A. 1925, Proc. of the Cambridge Philosophical Society, 22, 700
Fischer, D. A., Anglada-Escude, G., Arriagada, P., et al. 2016, PASP, 128, 066001
Fressin, F., Torres, G., Charbonneau, D., et al. 2013, ApJ, 766, 81
Fuhrmeister, B., Liefke, C., Schmitt, J. H. M. M., & Reiners, A. 2008, A&A, 487, 293
Fuhrmeister, B., Czesla, S., Schmitt, J. H. M. M., et al. 2018, A&A, in press, DOI: 10.1051/0004-6361/201732204

Garcia-Piquer, A., Morales, J. C., Ribas, I., et al. 2017, A&A, 604, A87
Gray, D. F. 2009, ApJ, 697, 1032
Halbwachs, J.-L., Arenou, F., Famaey, B., et al. 2014, in SF2A-2014: Proceedings of the Annual meeting of the French Society of Astronomy and Astrophysics, eds. J. Ballet, F. Martins, F. Bournaud, R. Monier, & C. Reylé, 427
Halverson, S., Terrien, R., Mahadevan, S., et al. 2016, in Ground-based and Airborne Instrumentation for Astronomy VI, Proc. SPIE, 9908, 99086P
Hatzes, A. P. 2002, Astron. Nachr., 323, 392
Hébrard, É. M., Donati, J.-F., Delfosse, X., et al. 2016, MNRAS, 461, 1465
Herrero, E., Ribas, I., Jordi, C., et al. 2016, A&A, 586, A131
Howard, A. W., Marcy, G. W., Bryson, S. T., et al. 2012, ApJS, 201, 15
Hung, H. M. J., O'Neill, R. T., Bauer, P., & Kohne, K. 1997, Biometrics, 53, 11
Jeffers, S. V., Barnes, J. R., Jones, H. R. A., et al. 2014, MNRAS, 438, 2717
Jeffers, S. V., Schöfer, P., Lamert, A., et al. 2018, A&A, 614, A76
Kürster, M., Endl, M., Rouesnel, F., et al. 2003, A&A, 403, 1077
Lovis, C., & Pepe, F. 2007, A&A, 468, 1115
Mayor, M., Pepe, F., Queloz, D., et al. 2003, The Messenger, 114, 20
Meunier, N., Desort, M., & Lagrange, A.-M. 2010, A&A, 512, A39
Meunier, N., Lagrange, A.-M., Mbemba Kabuiku, L., et al. 2017, A&A, 597, A52
Montes, D., Fernández-Figueroa, M. J., de Castro, E., & Cornide, M. 1995, A&A, 294, 165
Newton, E. R., Irwin, J., Charbonneau, D., et al. 2017, ApJ, 834, 85
Pecaut, M. J., & Mamajek, E. E. 2013, ApJS, 208, 9
Pepe, F., Molaro, P., Cristiani, S., et al. 2014, Astron. Nachr., 335, 8
Piskunov, N. E., & Valenti, J. A. 2002, A&A, 385, 1095
Press, W. H., Teukolsky, S. A., Vetterling, W. T., & Flannery, B. P. 2002, Numerical recipes in C++ : the art of scientific computing
Queloz, D., Henry, G. W., Sivan, J. P., et al. 2001, A&A, 379, 279
Quirrenbach, A., Amado, P. J., Caballero, J. A., et al. 2016, in SPIE Conf. Ser., Proc. SPIE, 9908, 990812
Redman, S. L., Lawler, J. E., Nave, G., Ramsey, L. W., & Mahadevan, S. 2011, ApJS, 195, 24
Reiners, A. 2009, A&A, 498, 853
Reiners, A., & Basri, G. 2007, ApJ, 656, 1121
Reiners, A., & Basri, G. 2008, ApJ, 684, 1390
Reiners, A., & Basri, G. 2010, ApJ, 710, 924
Reiners, A., Bean, J. L., Huber, K. F., et al. 2010, ApJ, 710, 432
Reiners, A., Joshi, N., & Goldman, B. 2012, AJ, 143, 93
Reiners, A., Shulyak, D., Anglada-Escudé, G., et al. 2013, A&A, 552, A103
Reiners, A., Mrotzek, N., Lemke, U., Hinrichs, J., & Reinsch, K. 2016, A&A, 587, A65
Reiners, A., Ribas, I., Zechmeister, M., et al. 2018a, A&A, 609, L5
Reiners, A., Zechmeister, M., Caballero, J. A., et al. 2018b, A&A, 612, A49
Ribas, I., Bolmont, E., Selsis, F., et al. 2016, A&A, 596, A111
Rousseeuw, P. J., & Croux, C. 1993, Journal of the American Statistical Association, 88, 1273
Saar, S. H., & Donahue, R. A. 1997, ApJ, 485, 319
Sarmiento, L. F., Reiners, A., Seemann, U., et al. 2014, in Ground-based and Airborne Instrumentation for Astronomy V, Proc. SPIE, 9147, 914754
Schäfer, S., & Reiners, A. 2012, in Ground-based and Airborne Instrumentation for Astronomy IV, Proc. SPIE, 8446, 844694
Semel, M. 1989, A&A, 225, 456
Suárez Mascareño, A., González Hernández, J. I., Rebolo, R., et al. 2017a, A&A, 597, A108
Suárez Mascareño, A., Rebolo, R., González Hernández, J. I., & Esposito, M. 2017b, MNRAS, 468, 4772
Tal-Or, L., Faigler, S., & Mazeh, T. 2015, A&A, 580, A21
Trifonov, T., Kürster, M., Zechmeister, M., et al. 2018, A&A, 609, A117
Vogt, S. S., Allen, S. L., Bigelow, B. C., et al. 1994, in SPIE Conf. Ser., 2198, 362
Winn, J. N., & Fabrycky, D. C. 2015, ARA&A, 53, 409
Wright, J. T. 2005, PASP, 117, 657
Young, A., Skumanich, A., Stauffer, J. R., Harlan, E., & Bopp, B. W. 1989, ApJ, 344, 427
Zechmeister, M., & Kürster, M. 2009, A&A, 496, 577
Zechmeister, M., Kürster, M., & Endl, M. 2009, A&A, 505, 859
Zechmeister, M., Anglada-Escudé, G., & Reiners, A. 2014, A&A, 561, A59
Zechmeister, M., Reiners, A., Amado, P. J., et al. 2018, A&A, 609, A12
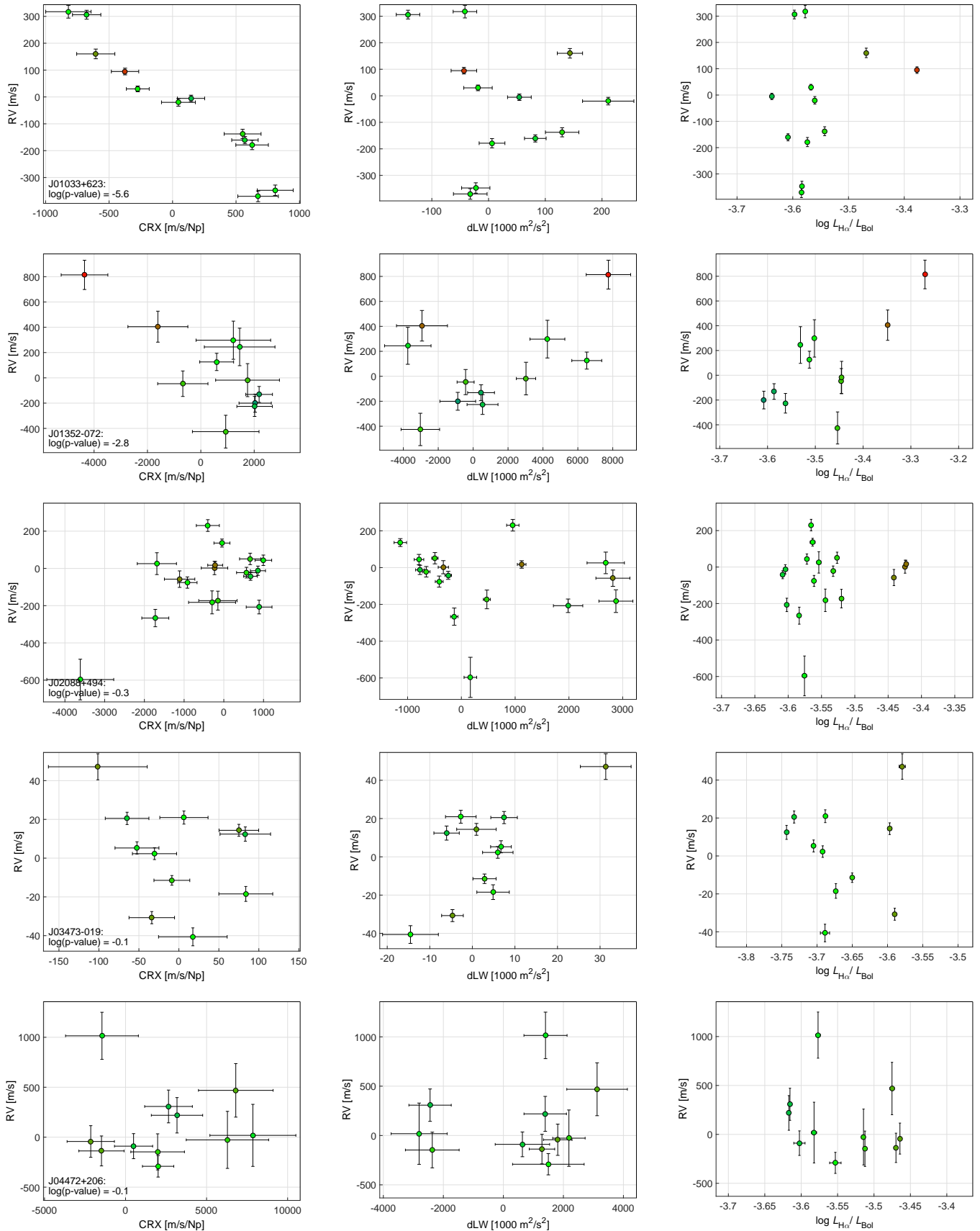
Appendix A: Additional figures

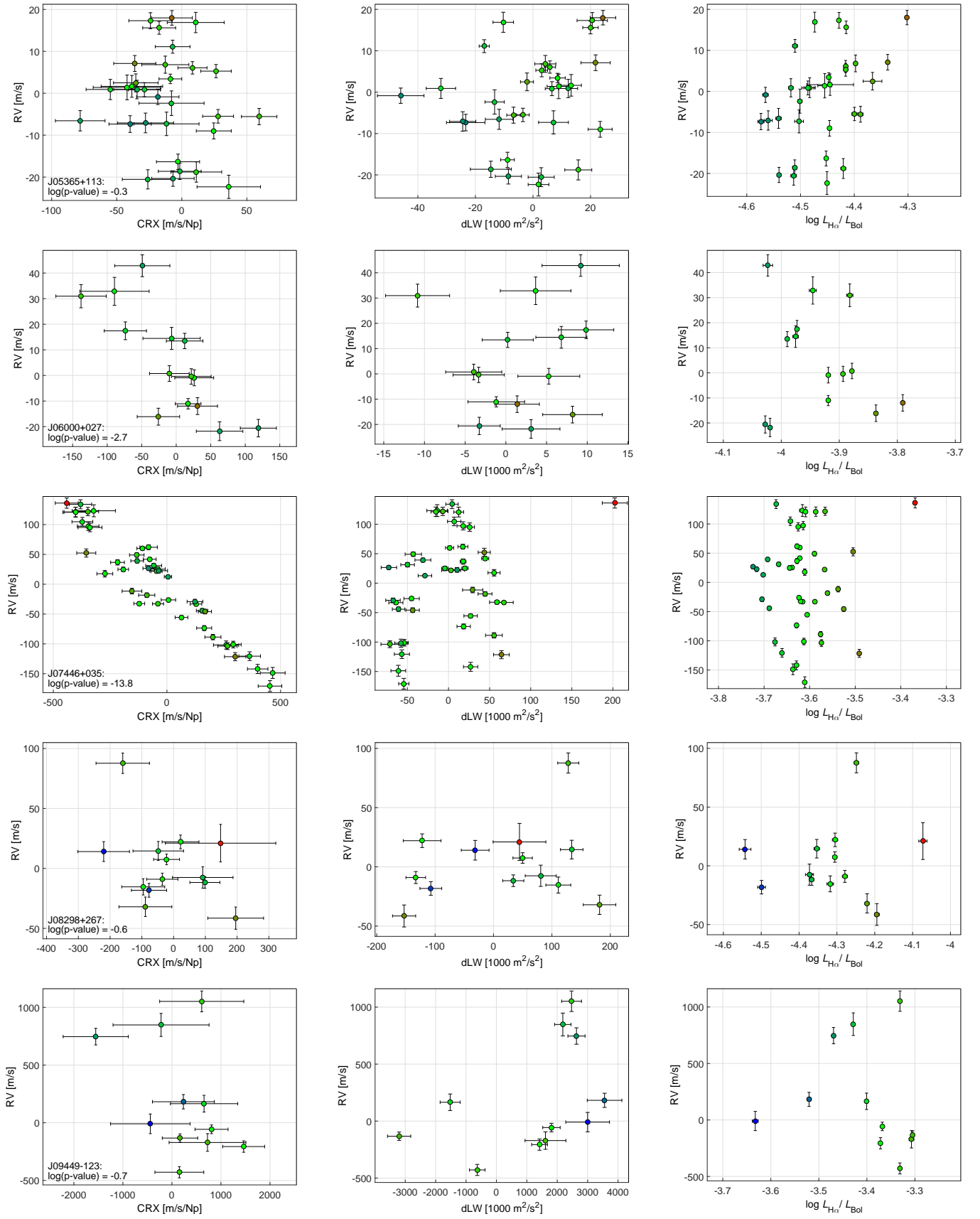**Fig. A.1.** Similar plots to Fig. 5 – one plot per RV-loud star.
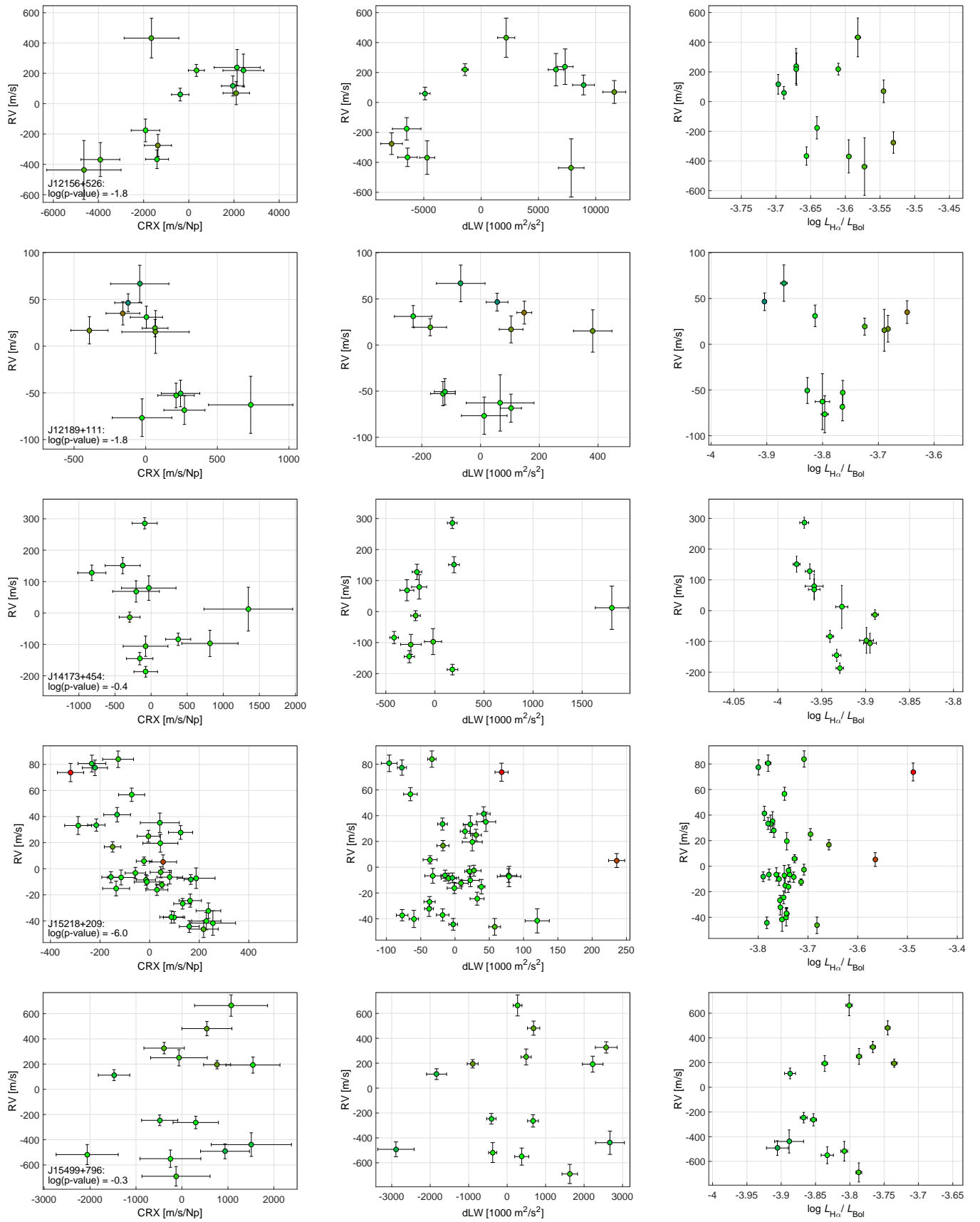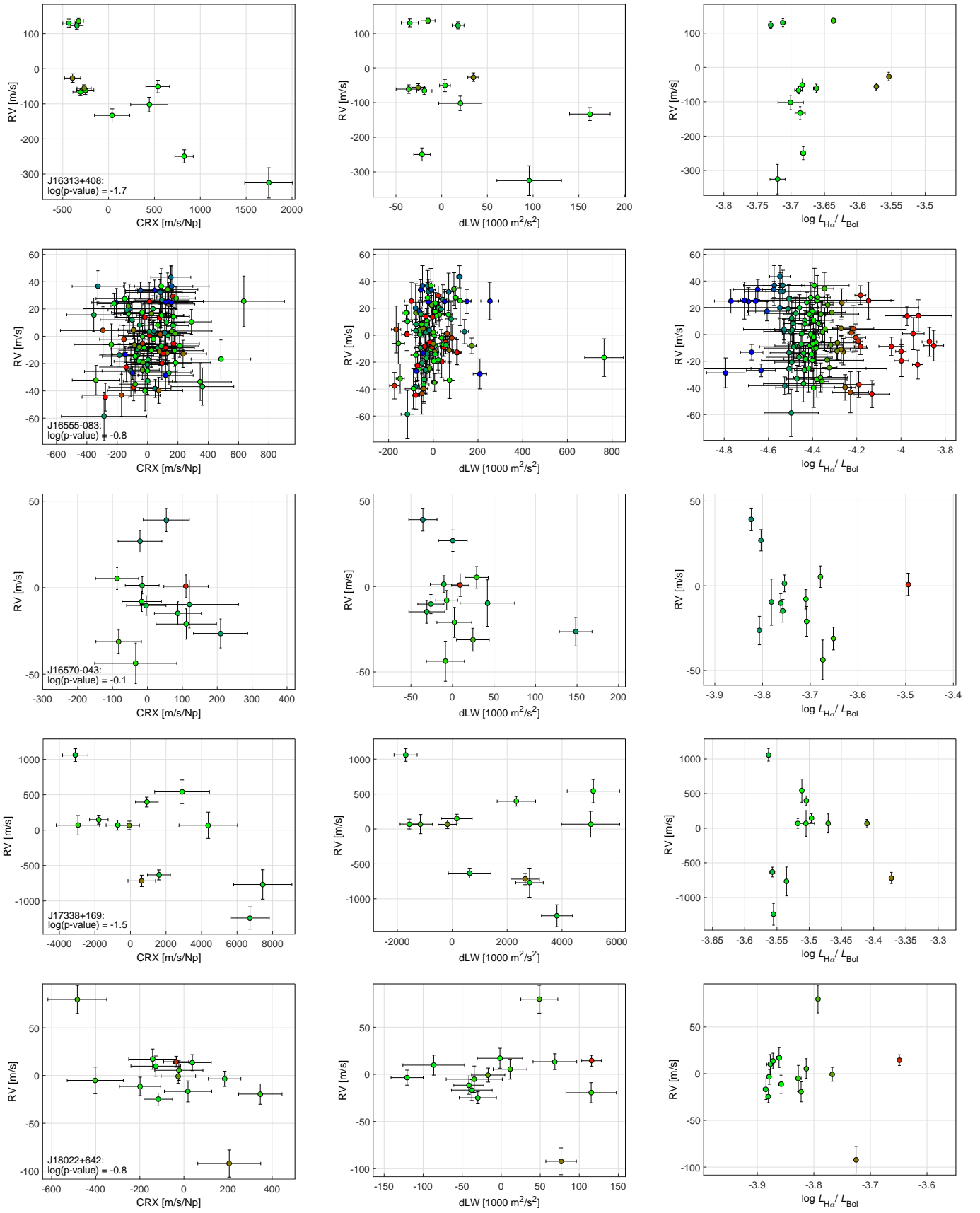
Fig. A.1. continued.

Fig. A.1. continued.

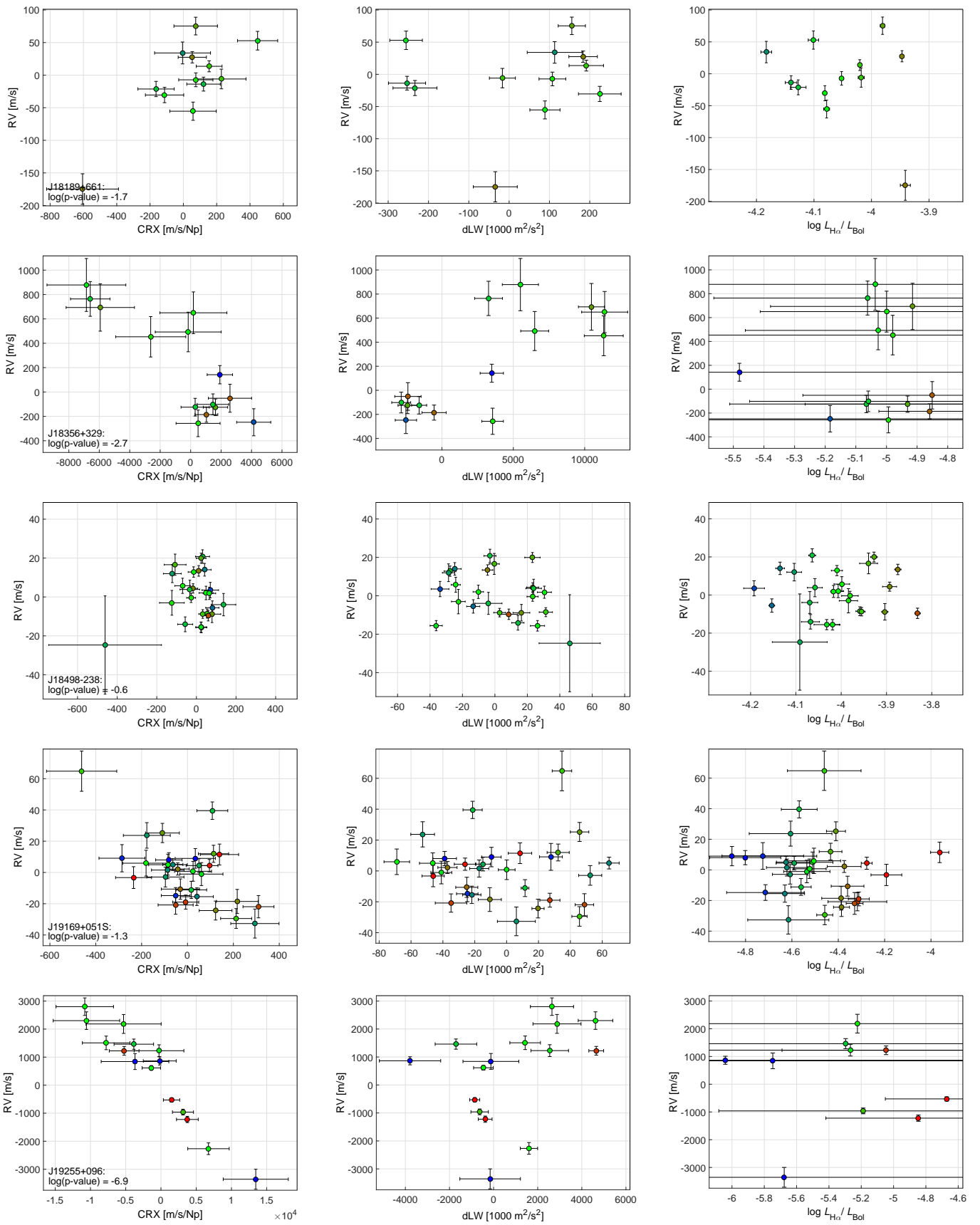**Fig. A.1.** continued.
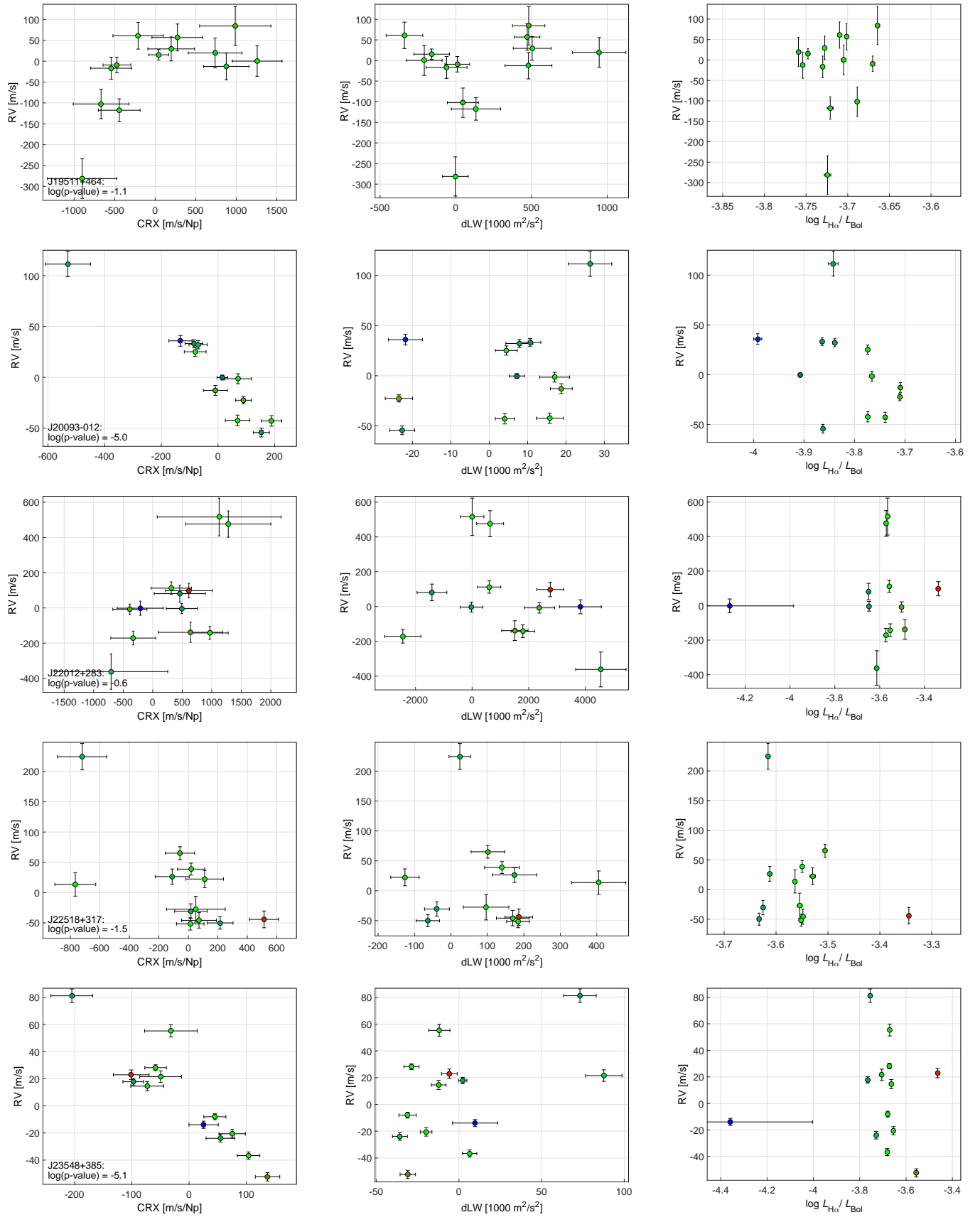
Fig. A.1. continued.

Fig. A.1. continued.